

Metamagnetic transitions and magnetoelectric responses in a chiral polar helimagnet $\text{Ni}_2\text{InSbO}_6$

Y. Araki,¹ T. Sato,¹ Y. Fujima,¹ N. Abe,¹ M. Tokunaga,² S. Kimura,³
D. Morikawa,⁴ V. Ukleev,⁴ Y. Yamasaki,^{4,5} C. Tabata,⁶ H. Nakao,⁷
Y. Murakami,⁷ H. Sagayama,⁷ K. Ohishi,⁸ Y. Tokunaga,¹ and T. Arima^{1,4}

¹*Department of Advanced Materials Science,
University of Tokyo, Kashiwa 277-8561, Japan*

²*Institute for Solid State Physics, University of Tokyo, Kashiwa 277-8581, Japan*

³*Institute for Materials Research, Tohoku University, Sendai 980-8577, Japan*

⁴*RIKEN Center for Emergent Matter Science (CEMS), Wako 351-0198, Japan*

⁵*Research and Service Division of Materials Data and Integrated System (MaDIS),
National Institute for Materials Science (NIMS), Tsukuba 305-0047, Japan*

⁶*Institute of Materials Structure Science,
High Energy Accelerator Research Organization, Tsukuba 305-0801, Japan*

⁷*Condensed Matter Research Center and Photon Factory,
Institute of Materials Structure Science High Energy Accelerator
Research Organization, Tsukuba 305-0801, Japan and*

⁸*Neutron and Technology Center, Comprehensive Research
Organization for Science and Society (CROSS), Tokai 319-1106, Japan*

(Dated: April 8, 2024)

Abstract

Magnetic-field effect on the magnetic and electric properties in a chiral polar ordered corundum $\text{Ni}_2\text{InSbO}_6$ has been investigated. Single-crystal soft x-ray and neutron diffraction measurements confirm long-wavelength magnetic modulation. The modulation direction tends to align along the magnetic field applied perpendicular to the polar axis, suggesting that the nearly proper-screw type helicoid should be formed below 77 K. The application of a high magnetic field causes a metamagnetic transition. In a magnetic field applied perpendicular to the polar axis, a helix-to-canted antiferromagnetic transition takes place through the intermediate soliton lattice type state. On the other hand, a magnetic field applied along the polar axis induces a first-order metamagnetic transition. These metamagnetic transitions accompany a change in the electric polarization along the polar axis.

I. INTRODUCTION

Noncentrosymmetric magnets often host non-collinear or non-coplanar spin arrangements, such as magnetic helices, solitons, and skyrmions^{1,2}. For instance, magnetic helix, cone, Bloch-type-skyrmion lattice, and chiral soliton lattice have been reported in B20-type compounds³, β -Mn-type Co-Zn-Mn alloys⁴, and Cu_2OSeO_3 ⁵ with chiral cubic structures. Néel-type-skyrmion lattice is observed in polar magnets, such as GaV_4S_8 ⁶, GaV_4Se_8 ⁷, and VOSe_2O_5 ⁸. Furthermore, antiskyrmions appear in magnets with D_{2d} -symmetry⁹. The skyrmion lattices in insulating materials, such as Cu_2OSeO_3 and GaV_4S_8 have been found to accompany the magnetoelectric (ME) coupling^{10,11}. The cross-correlation response attracts interest in terms of the electric-field control of magnetic structure, in particular topological magnetic objects.

To explore a colossal ME response with specific spin ordering, magnetic oxides of Ni_3TeO_6 -type chiral polar ordered corundum structure with a space group $R\bar{3}$ may be good candidates¹². Ni_3TeO_6 undergoes an antiferromagnetic transition at 52 K¹³. Below the Néel temperature, the material shows colossal ME effects across two-step spin-flop transitions^{14–16}. The present study focuses on isostructural $\text{Ni}_2\text{InSbO}_6$, which is obtained by substitution of In^{3+} and Sb^{5+} for one third of Ni^{2+} and Te^{6+} , respectively. The lattice parameters are $a = 5.2168 \text{ \AA}$ and $c = 14.0166 \text{ \AA}$ in the hexagonal notation (we use in the hexagonal notation in this paper). While Ni moments in Ni_3TeO_6 are collinearly arranged in the antiferromagnetic phase, $\text{Ni}_2\text{InSbO}_6$ hosts an incommensurate helimagnetic modulation with a propagation vector $\mathbf{q} = (0, 0.029, 0)$ below $T_N = 76 \text{ K}$, according to the powder neutron diffraction¹⁷. The long helimagnetic period suggests that Dzyaloshinskii-Moriya (DM) interaction should be essential for the helimagnetic order. The helimagnetically ordered Ni planes are stacked along the c -axis in the out-of-phase manner as in $\text{Fe}_3\text{PO}_4\text{O}_3$ ¹⁸. Due to the noncentrosymmetric nature of the underlying crystal structure with both chirality and polarity, $\text{Ni}_2\text{InSbO}_6$ can exhibit a unique magnetic property and fascinating ME responses. As reported in Ref.¹⁹, DM interaction activated in a C_3 -symmetry magnet can work differently from that in polar or chiral magnets. $\text{Ni}_2\text{InSbO}_6$ is a rare example which belongs to C_3 point group and hosts non-collinear spiral spin ordering.

Here, we study physical properties of $\text{Ni}_2\text{InSbO}_6$ by using single crystals. Since a spin helix shows an anisotropic response to an external field in general, experimental research by

using single crystalline samples is essential to clarify the multiferroic property of the unique spin spiral order²⁰. We have found that large pyroelectricity is induced by the helimagnetic order. Metamagnetic transitions are observed by measurements of magnetization, electric polarization, and a dielectric constant in high magnetic fields.

II. EXPERIMENTAL

Single crystals of $\text{Ni}_2\text{InSbO}_6$ were grown by the chemical vapor transport method with use of PtCl_2 as the transport agent²¹. The c -plane was easily grown, resulting in plate-shaped crystals. The typical dimensions of obtained crystals were 1-3 mm² in area and 500 μm thick. Polarized light microscopy clarified that they had chiral twins, as reported in²². Since it was reported that Ni_3TeO_6 , which has a similar structure, hosted composite domain walls of chirality and polarity²³, the measurement of electric polarization along the c -axis was carried out on a homochiral domain, whose area was 0.74 mm² by the integration of displacement current measured by an electrometer (6517A, Keithley). Dielectric constants were measured by using an LCR meter (E4980A, Agilent). Magnetization was measured by a superconducting quantum interference device magnetometer (MPMS-XL, Quantum Design). High magnetic-field measurements of magnetization and electric polarization were performed with use of a pulse magnet at the Institute for Solid State Physics, the University of Tokyo. Dielectric constant measurements in steady high magnetic fields were performed at the High Field Laboratory for Superconducting Materials, Institute for Materials Research, Tohoku University. Small-angle soft x-ray scattering (SAXS) measurements at Ni L_3 absorption edge were performed on BL-16A and 19B, Photon Factory, KEK, Japan. The experimental setup for the SAXS measurements is schematically shown in Fig. 2(a) (see Refs.^{24,25} for details). A plate of $\text{Ni}_2\text{InSbO}_6$ crystal of a thickness of about 300 nm was fabricated by using a focused ion beam thinning method. The thin-plate sample was put on a Si_3N_4 membrane covered by a gold film with a pin hole of 5 μm in diameter as depicted in Fig. 2(b). We used left-handed circularly polarized and unpolarized x-ray at BL-16A and BL-19B, respectively. 853-eV (Ni L_3 edge) soft x-ray was irradiated on the sample and the scattered x-ray near the transmitted beam was recorded by a charge-coupled detector (CCD) camera. A time-of-flight neutron scattering measurement was carried out on three crystals aligned on an Al plate on BL15 in MLF, J-PARC, Japan²⁶. Small- and wide-angle neutron scattering were

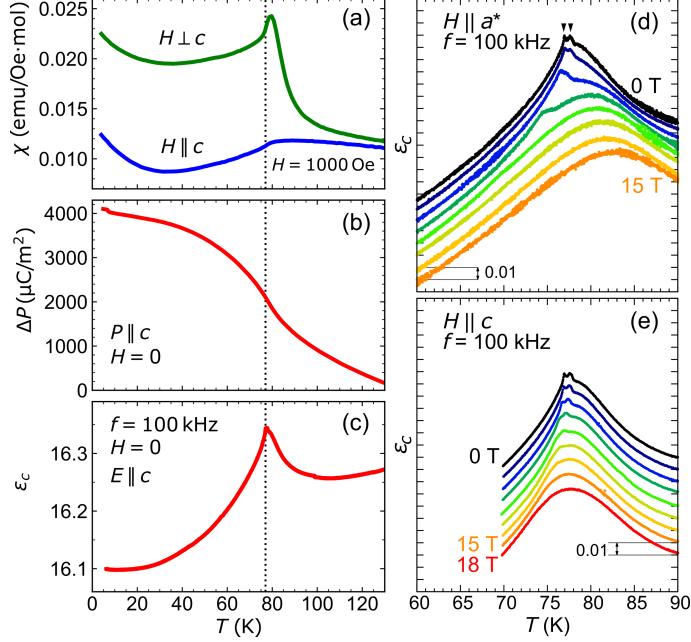


FIG. 1. Temperature dependence of (a) magnetic susceptibility χ , (b) change in electric polarization ΔP , and (c) electric permittivity ϵ_c along the c -axis at a frequency 100 kHz. A dotted line shows a magnetic transition at 77 K. (d)(e) Temperature dependence of ϵ_c in magnetic fields of 0 T, 2 T, 4 T, 6 T, 8 T, 10 T, 12 T, 15 T for (d) $\mathbf{H} \parallel \mathbf{a}^*$ and (e) $\mathbf{H} \parallel \mathbf{c}$. 18-T data are also added for $\mathbf{H} \parallel \mathbf{c}$. Data are vertically offset for clarity.

recorded by position sensitive detectors.

III. FUNDAMENTAL PHYSICAL PROPERTIES

Figure 1 shows fundamental physical properties of $\text{Ni}_2\text{InSbO}_6$ as functions of temperature T . Magnetic susceptibility shows an anomaly at $T_N = 77$ K. The temperature approximately agrees with the previously reported magnetic transition temperature¹⁷. Weiss temperature θ_W is estimated to be -207 K and -188 K by using the susceptibility data above 150 K (not shown) for magnetic fields $\mathbf{H} \perp \mathbf{c}$ and $\mathbf{H} \parallel \mathbf{c}$ respectively. The frustration parameter $|\theta_W/T_N|$ is smaller than 3, implying that the helimagnetic order should not originate from magnetic frustration but from DM interaction. Figure 1(b) describes that the electric polarization shows a steep change at around T_N superposed on large pyroelectricity purely due to the polar nature of the crystal. The change in the electric polarization between T_N and the lowest temperature is approximately $2000 \mu\text{C}/\text{m}^2$. This value is almost comparable

to Ni_3TeO_6 ¹⁴ and larger than the typical value of the order of $\mu\text{C}/\text{m}^2$ in other multiferroic materials²⁷.

Figures 1(d) and (e) display temperature dependence of electric permittivity ϵ_c along the c -axis around T_N in various magnetic fields. A double peak structure is observed around T_N in zero field, as indicated by black triangles, which suggests two-step successive phase transitions. An in-plane magnetic field $\mathbf{H} \parallel \mathbf{a}^*$ shifts the low-temperature anomaly to lower temperatures. The anomaly becomes less prominent with increasing the magnetic field. In contrast, a magnetic field along the c -axis only broadens the anomaly, as shown in Fig. 1(e).

IV. SMALL-ANGLE RESONANT SOFT X-RAY MAGNETIC SCATTERING

A SAXS measurement in resonant with Ni L_3 absorption edge was performed with the incident x-ray propagating in the c -direction. Ring-like scattering in the c -plane is observed at 50 K (below T_N) after zero-field cooling, as shown in Fig. 2(c). Note that the shadow of a direct beam catcher is seen at the center of the image. The diffraction disappears at 85 K (above T_N), as shown in Fig. 2(d), suggesting its magnetic origin. Figure 2(e) shows the intensity profiles along $|\mathbf{q}|$ at an azimuthal angle $\phi = -127.5^\circ$. By pseudo-Voigt fitting of the profile along the radial direction after zero-field cooling, the position and the half width of half maximum of the superlattice peak are estimated to be $4.15 \times 10^{-1} \text{ nm}^{-1}$ and $5.73 \times 10^{-3} \text{ nm}^{-1}$, respectively. The sharp peak profile indicates the well-defined period $\lambda = 15 \pm 1 \text{ nm}$ of the helimagnetic order, which is in accord with the previous report¹⁷. Four-fold like intensity distribution is observed in the azimuthal dependence of the zero-field cooling pattern, as shown in Figs. 2(c) and 2(f), although $\text{Ni}_2\text{InSbO}_6$ has the C_3 symmetry. This discrepancy may arise from some strain in the thin-plate sample and the boundary condition of the square-shaped sample, shown in Fig. 2(b). The modulation direction can be controlled by a magnetic-field cooling. Figure 2(f) compares the intensity profile along the azimuthal angle ϕ in zero magnetic field at 50 K after zero magnetic field cooling with that after the sample was cooled from above T_N in a magnetic field $\mu_0 H = 0.4 \text{ T}$ in the direction of $\phi = 45^\circ$. The scattering intensities around $\phi \simeq -135^\circ$ and 45° , which locate along the field direction, are increased after the field-cooling procedure, while those around $\phi \simeq -45^\circ$ and 135° are decreased. Considering the fact that a magnetic field tends to rotate the propagation direction of the helix so that the spiral plane becomes normal to the magnetic

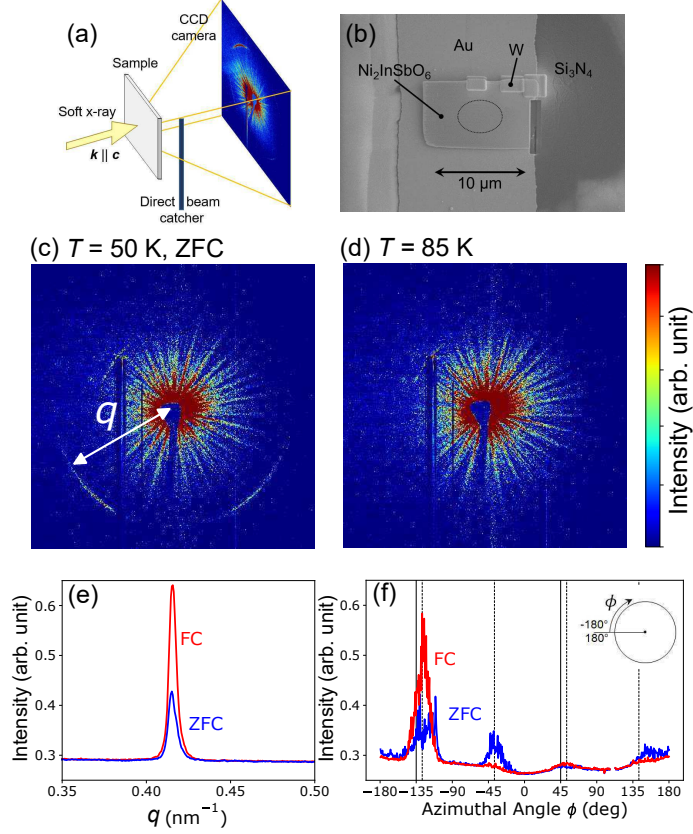


FIG. 2. Small angle resonant soft x-ray scattering of $\text{Ni}_2\text{InSbO}_6$ for the incident x-ray propagating parallel to the c -axis. (a) Schematic image of experimental setup for SAXS measurements. (b) Thin plate fabricated by a focused ion beam process on a gold-coated Si_3N_4 membrane. The dotted line indicates a position of the precise circle shaped pinhole. (c)(d) Diffraction patterns in zero magnetic field at (c) 50 K (below T_N) and (d) 85 K (above T_N). (e) Intensity profiles of x-ray scattering along the radial direction q at 50 K. The intensity is obtained by the integration in the range of $-142.5^\circ < \phi < -112.5^\circ$. (f) Intensity profiles of x-ray scattering along the azimuthal direction at 50 K for $0.406 \text{ nm}^{-1} < |q| < 0.423 \text{ nm}^{-1}$. The inset describes the definition of azimuthal angle ϕ . Two Solid lines show magnetic field direction, which is positioned at $\phi = -135^\circ$ and 45° .

field direction to maximize the Zeeman-energy gain, the observed field-cooling effect implies that the helimagnetic order should be nearly proper-screw type. The chiral component of DM interaction (DM vector parallel to the bond) should be dominant over the polar one (DM vector normal to the bond).

V. NEUTRON DIFFRACTION

The effect of a magnetic field on the helicoid is also confirmed by neutron scattering. Figure 3 illustrates a contour map of the intensity of neutron diffraction on the two-dimensional reciprocal ($hk3$) plane. Ring-like scattering is observed around (003) reflection at 60 K (below T_N) and disappears at 80 K (above T_N). The ring shape indicates that the direction of the modulation vector \mathbf{q} of helimagnetic order in the bulk sample should be distributed isotropically in the c -plane. The period of magnetic modulation is estimated to be about 15.7 nm, which agrees with the previous report¹⁷ as well as the present SAXS result. The application of a magnetic field of 6 T along the a^* -axis at 60 K concentrates the intensity of the magnetic diffraction along the field (Fig. 3(b)), which is again in accord with the SAXS result. Figure 3(d) shows the temperature dependence of (003) and satellite intensities at 6 T. The (003) intensity reaches the maximum just below T_N , and decreases above 80 K. On the other hand, the satellite intensity is decreased with a rise of temperature, and is almost the same as the background level above 80 K. These behaviors well correspond to the anomalies of dielectric constant in a magnetic field of 6 T, as depicted in Fig. 3(e). The system may first undergo a magnetic transition to the commensurate layered antiferromagnetic phase upon cooling and then successively enter the helical phase with a long-wavelength modulation below 74 K.

VI. PULSE MAGNET MEASUREMENT

Figure 4 shows high-field M - H and P - H curves at various temperatures measured by using a pulse magnet. For $\mathbf{H} \perp \mathbf{c}$, the M - H curves below T_N have a clear anomaly, as shown in Fig. 4(a). The transition field H_c is approximately 14 T at 4.2 K, decreases monotonically with a rise in temperature, and disappears above T_N , as in the curve at 85 K. The magnetization below H_c is superlinear to the field, which could be featured by soliton lattice formation, as discussed later. The magnetization in a higher-field phase below T_N is linear to the magnetic field, and the extrapolation to $\mu_0 H = 0$ T remains non-zero ($0.17 \mu_B/\text{Ni}$ at 4.2 K), suggesting that the higher-field phase should essentially have a spontaneous magnetization component. The extrapolation value decreases monotonically with an increase of temperature. For $\mathbf{H} \parallel \mathbf{c}$, a metamagnetic transition takes place with a hysteresis loop, which

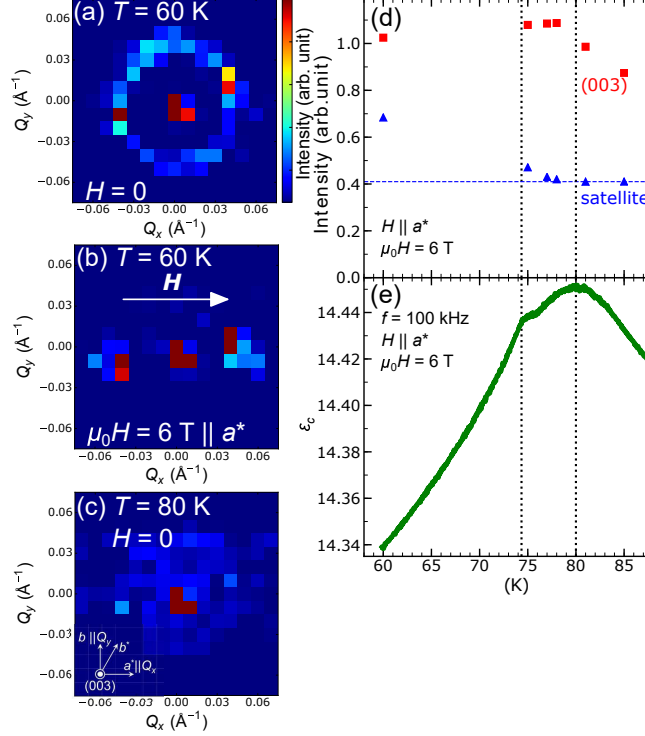


FIG. 3. Neutron scattering patterns in the $(hk3)$ plane. Q_x and Q_y are along a^* - and b -axes, respectively. The inset in (c) shows the reciprocal crystal axes in the experimental setup. (a) Scattering pattern at 0 T and 60 K. (b) Scattering pattern at $\mu_0 H = 6$ T and 60 K. The magnetic field was applied along the a^* -axis before the sample was cooled down to the ordered phase. (c) Scattering pattern at 80 K (above T_N) (d) The temperature dependence of the intensity of (003) and satellite diffractions described as red squares and blue triangles, respectively. The background level of satellite diffractions is depicted as a blue horizontal broken line determined by the scattering intensity at 85 K (far above T_N). (e) The temperature dependence of dielectric constant in a magnetic field $\mu_0 H$ of 6 T along the a^* -axis. The vertical dot lines indicate the temperature where dielectric anomalies appear.

is completely different from the case of $\mathbf{H} \perp \mathbf{c}$ configuration, as shown in Fig. 4(c). The transition field increases and the hysteresis loop becomes smaller with a rise of temperature. As in the case of $\mathbf{H} \perp \mathbf{c}$ configuration, the field-induced magnetic transition disappears above T_N .

As shown in Figs. 4(b) and (d), the change in electric polarization shows an anomaly at the metamagnetic transition. The electric polarization below T_N is almost insensitive to the magnetic field perpendicular to the c -axis in the low-field phase, while in the high-field

phase, it shows parabolic dependence on magnetic field. Around T_N , the sign of the ME coefficient is reversed, and the parabolic dependence disappears. The value of ΔP_c at each temperature in the high field phase is in the order of $10 \text{ } \mu\text{C}/\text{m}^2$, which is much smaller than the pyroelectricity at zero-field. The ME effect remains even above T_N . The electric polarization shows quadratic dependence on magnetic field for $\mathbf{H} \parallel \mathbf{c}$ in both low and high fields. The typical value is comparable with that in the $\mathbf{H} \perp \mathbf{c}$ configuration. The quadratic ME effect is observed up to 200 K. The sign of the ME effect does not change in the whole temperature range, which is different from the case of $\mathbf{H} \perp \mathbf{c}$.

VII. MAGNETIC PHASE DIAGRAM

Based on the dielectric constant, electric polarization, and magnetization data as well as SAXS and neutron diffraction profiles, we propose magnetic phase diagrams of $\text{Ni}_2\text{InSbO}_6$, as shown in Figs. 5 (a) and (b). The gray and pink areas indicate the helical and paramagnetic phases, respectively, as previously reported in¹⁷. A small green pocket “A” between helical and paramagnetic phases is revealed by the dielectric property. The nature of this phase is still unknown, because SAXS and neutron diffraction intensities are too weak to analyze. The phases displayed by blue and yellow areas are discovered in the present high-field measurements.

VIII. DISCUSSIONS

We discuss the variations in the magnetic structure of $\text{Ni}_2\text{InSbO}_6$. We assign the low-field phase in the $\mathbf{H} \perp \mathbf{c}$ configuration below H_c to the soliton lattice phase with modulating the nearly proper-screw type helicoid (Fig. 4(e)), as signaled in the superlinear M - H curve (Fig. 4(a)). As shown in Fig. 3(b), the \mathbf{q} -direction is aligned nearly along the external field in $\text{Ni}_2\text{InSbO}_6$ below several tesla. With increasing the magnetic field, the helical structure is gradually modified in the $\mathbf{H} \parallel \mathbf{q}$ configuration. In a chiral ferromagnet with uniaxial \mathbf{q} , chiral-soliton lattice can be formed in the $\mathbf{H} \perp \mathbf{q}$ configuration²⁸. On the other hand, the formation of solitons in a magnetic field is not straightforward in a chiral antiferromagnet. Above a critical field H_c , weak-ferromagnetic structure should appear as is the case in BiFeO_3 ^{29,30}. To explain the emergence of the soliton and weak-ferromagnetic phase in the

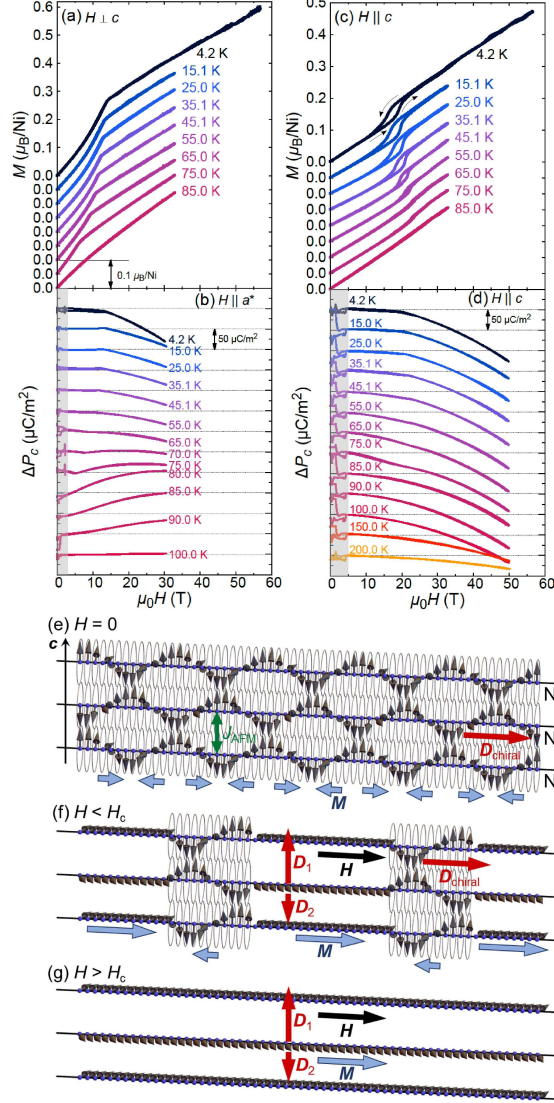


FIG. 4. (a)(c) Magnetization curves at various temperatures in (a) $\mathbf{H} \perp \mathbf{c}$ and (c) $\mathbf{H} \parallel \mathbf{c}$ configurations. (b)(d) Magnetic-field dependence of the change in electric polarization ΔP_c along the c -axis at various temperatures in (b) $\mathbf{H} \parallel \mathbf{a}^*$ and (d) $\mathbf{H} \parallel \mathbf{c}$ configurations. Anomalies in the shaded area at low fields are due to electric noise of the ignition of the pulse magnet. M - H and P - H curves in (a)-(d) are vertically offset for clarity. (e)-(g) Schematic drawing of the possible magnetization process in $\mathbf{H} \perp \mathbf{c}$. For simplicity, polarity-induced uniform DM interaction is neglected. (e) Proper-screw helicoid in zero field. (f) Intermediate soliton lattice state induced by a moderate magnetic field $H < H_c$. (g) Weak-ferromagnetic structure in a magnetic field higher than the critical field H_c .

$\mathbf{H} \perp \mathbf{c}$ configuration, we take into account an additional alternate DM interaction, because neither chirality- nor polarity-induced uniform DM interaction can drive the spontaneous magnetization. In the present system, layers formed by crystallographically non-equivalent two Ni sites, namely Ni1 and Ni2, stack alternately along the c -axis. Here we consider the interaction between Ni moments on neighboring layers. In addition to the antiferromagnetic symmetric exchange, the lack of inversion center allows antisymmetric exchange interactions. The essential component of the DM vector is along the c -axis, which should alternately change the value. Here we show alternating component, represented by DM vectors \mathbf{D}_1 and \mathbf{D}_2 along the c -axis with the opposite signs to each other, as shown in Fig. 4(g)³¹. The DM vectors make magnetic moments on Ni1 and Ni2 noncollinear if Ni moments are in the c -plane, while the antisymmetric exchange is inactive if Ni moments are along the c -axis. Therefore, when the Ni moments are arranged to form layered antiferromagnetic structure, a uniform canted weak-ferromagnetic component can emerge in the c -plane. This situation is expected to realize above the critical field H_c , as shown in Fig. 4(g). Here, the weak-ferromagnetic component roughly orients in the \mathbf{H} -direction. When the magnetic field is reversed, the weak-ferromagnetic moment flips, which should accompany the reversal of the sublattice moment. At $H = 0$, on the other hand, the staggered DM vectors induce local weak-ferromagnetic moments at positions where Ni moments have the c -plane components on the proper-screw structure. These local weak-ferromagnetic components are along the \mathbf{q} -direction, and bring about sinusoidal modulation in the original proper-screw structure (Fig. 4(e)). Hence, the application of a magnetic field in the c -plane modulates the sinusoid (and thus the underlying proper-screw structure) so that the regions which have local weak-ferromagnetic moment parallel (antiparallel) to the field expand (shrink) to acquire Zeeman energy gain, resulting in the formation of the soliton structure, as shown in Fig. 4(f).

On the contrary, the isothermal magnetization curve in the $\mathbf{H} \parallel \mathbf{c}$ configuration is almost linear below the critical field. The difference between two magnetic field configurations can be caused whether the local weak-ferromagnetic component is stabilized by DM interaction. The nature of the observed field-induced magnetic transition in $\mathbf{H} \parallel \mathbf{c}$ configuration is not clear in the present stage. Conical structure with the modulation along the c -axis may appear in a high external magnetic field along c -axis as in Co doped $\text{Ni}_2\text{ScSbO}_6$ ³². Another possible scenario is that a simple canted layered antiferromagnetic structure is induced similarly to the case of $\mathbf{H} \perp \mathbf{c}$.

The temperature dependence of electric polarization is shown in Fig. 1(b). The proper-screw type helicoid drives considerably large pyroelectricity. To consider the origin of the ME properties, we take inverse DM mechanism³³, exchange striction, and spin-direction dependent p - d hybridization³⁴ into account. The inverse DM effect cannot work effectively in proper-screw helicoid. The electric polarization driven by the exchange striction mechanism ΔP_z^{ex} is expressed as

$$\Delta P_z^{\text{ex}} = C \mathbf{S}_{\text{Ni1}} \cdot \mathbf{S}_{\text{Ni2}}. \quad (1)$$

The pyroelectricity measurement shows that the antiferromagnetic arrangement between \mathbf{S}_{Ni1} and \mathbf{S}_{Ni2} enhances the polarization. Therefore the coefficient C should be negative if the exchange striction is dominant. In the proposed weak-ferromagnetic structure as described in Fig. 4(g), Ni1 and Ni2 moments can be represented as $\mathbf{S}_{\text{Ni1}} = (S_x, S_y, 0)$ and $\mathbf{S}_{\text{Ni2}} = (S_x, -S_y, 0)$, where x is the magnetic-field direction and y is set in the c -plane. The exchange striction is calculated to be $C(-S^2 + 2S_x^2)$, where S is the value of Ni spin moment.

To calculate the contribution of p - d hybridization mechanism to the electric polarization in a NiO_6 octahedral cluster with 3-fold rotational symmetry, we set six unit vectors $\mathbf{e}_{ij}^{\text{NiO}}$ along the Ni-O bonds as

$$\begin{aligned} \mathbf{e}_{11}^{\text{NiO}} &= \begin{pmatrix} \sin \theta_1 \cos \phi_1 \\ \sin \theta_1 \sin \phi_1 \\ \cos \theta_1 \end{pmatrix}, \quad \mathbf{e}_{12}^{\text{NiO}} = \begin{pmatrix} \sin \theta_1 \cos (\phi_1 + \frac{2}{3}\pi) \\ \sin \theta_1 \sin (\phi_1 + \frac{2}{3}\pi) \\ \cos \theta_1 \end{pmatrix}, \\ \mathbf{e}_{13}^{\text{NiO}} &= \begin{pmatrix} \sin \theta_1 \cos (\phi_1 - \frac{2}{3}\pi) \\ \sin \theta_1 \sin (\phi_1 - \frac{2}{3}\pi) \\ \cos \theta_1 \end{pmatrix}, \quad \mathbf{e}_{21}^{\text{NiO}} = \begin{pmatrix} \sin \theta_2 \cos \phi_2 \\ \sin \theta_2 \sin \phi_2 \\ \cos \theta_2 \end{pmatrix}, \\ \mathbf{e}_{22}^{\text{NiO}} &= \begin{pmatrix} \sin \theta_2 \cos (\phi_2 + \frac{2}{3}\pi) \\ \sin \theta_2 \sin (\phi_2 + \frac{2}{3}\pi) \\ \cos \theta_2 \end{pmatrix}, \\ \mathbf{e}_{23}^{\text{NiO}} &= \begin{pmatrix} \sin \theta_2 \cos (\phi_2 - \frac{2}{3}\pi) \\ \sin \theta_2 \sin (\phi_2 - \frac{2}{3}\pi) \\ \cos \theta_2 \end{pmatrix}, \end{aligned} \quad (2)$$

where the index i denotes whether the oxygen positions upward ($i = 1$) or downward ($i = 2$) Ni. The index j denotes 3-fold symmetric Ni-O bonds in the c -plane. The values of ϕ_1, ϕ_2, θ_1

and θ_2 are 65.9° , 4.5° , 48.7° , and 115.9° for the Ni1-O cluster and 1.5° , 54.1° , 49.2° , and 120.6° for the Ni2-O cluster, respectively¹⁷. The change in the electric polarization induced by spin-direction dependent p - d hybridization mechanism ΔP_z^{pd} is given by

$$\Delta P_z^{pd} \propto \sum_{i,j} (\mathbf{S}_{\text{Ni}} \cdot \mathbf{e}_{ij}^{\text{NiO}})^2 e_{ijz}^{\text{NiO}} \quad (3)$$

$$= A(S_x^2 + S_y^2) + BS_z^2 \quad (4)$$

$$= AS^2 + (B - A)S_z^2, \quad (5)$$

where A and B are constants. This formula indicates that only the z -component of magnetic moment can affect P_z . The z -component of magnetization fluctuates around T_N . The P_z value should change when the external magnetic field suppresses the fluctuation and modifies $\langle S_z^2 \rangle$. The sign of ΔP_z^{ex} is negative both for $\mathbf{H} \parallel \mathbf{c}$ and for $\mathbf{H} \perp \mathbf{c}$ while that of ΔP_z^{pd} is positive for $\mathbf{H} \perp \mathbf{c}$ but negative for $\mathbf{H} \parallel \mathbf{c}$. The field dependence of electric polarization is shown in Fig. 4(b) at 70-90 K. At lower temperatures, it seems that the change in electric polarization is dominated by exchange striction mechanism, because $S_z = 0$ and thus $\Delta P_z^{pd} \simeq 0$ in the field-induced weak-ferromagnetic phase. On the other hand, for $\mathbf{H} \parallel \mathbf{c}$, S_z is modified as H is increased and thus $\Delta P_z^{pd} \neq 0$. The magnetization is approximately proportional to the field in each magnetic phase. Therefore, the electric polarization driven by p - d hybridization should show quadratic H -dependence as in the case of the exchange striction, which agrees with the experimental observation.

IX. CONCLUSION

We have found giant pyroelectricity in $\text{Ni}_2\text{InSbO}_6$ driven by helimagnetic order. A peculiar magnetization curve in the $\mathbf{H} \perp \mathbf{c}$ configuration suggests soliton-like magnetic modulation. We propose that 2π solitons may be created in the canted antiferromagnetic background. The application of a magnetic field along c -axis triggers a metamagnetic transition with a hysteresis loop. Further neutron scattering study is necessary to pin down the magnetic structure at each phase.

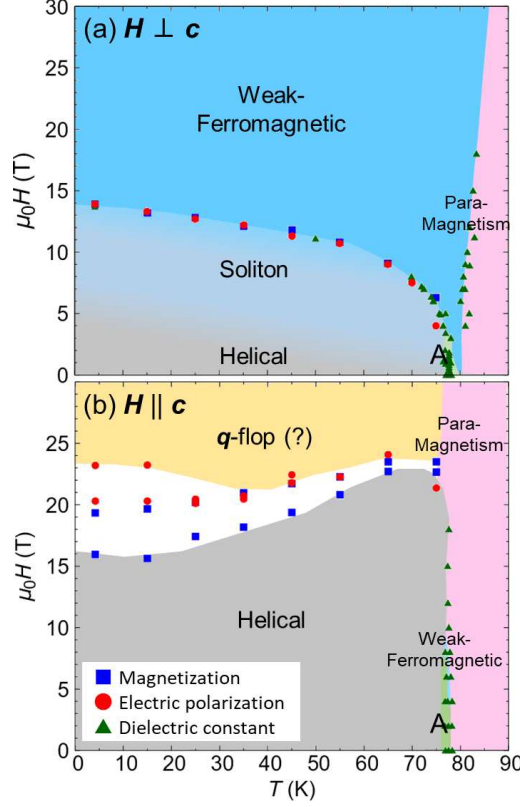


FIG. 5. Magnetic phase diagrams of $\text{Ni}_2\text{InSbO}_6$ proposed by macroscopic and quantum beam measurements in configurations (a) $\mathbf{H} \perp \mathbf{c}$ and (b) $\mathbf{H} \parallel \mathbf{c}$. A white area which is located between blue and yellow areas in $\mathbf{H} \parallel \mathbf{c}$ configuration shows the hysteresis loop (upper and lower points are obtained in the field-increasing and -decreasing processes, respectively).

X. ACKNOWLEDGEMENTS

This work was partly supported by JSPS KAKENHI Grants No.s JP25220803, JP16H01065, JP16K13828, JP19H01835, and JP19H05826. Y.A., T.S. and Y.F. are supported by Japan Society for the Promotion of Science (JSPS) through Program for Leading Graduate Schools(MERIT). The measurements of magnetization, electric polarization, and x-ray Laue photograph were performed by using facilities of the Institute for Solid State Physics (ISSP), the University of Tokyo. The authors thank T. Yajima for assistance in the XRD experiment at ISSP. Measurements in steady high magnetic fields were performed in the High Field Laboratory for Superconducting Materials, Institute for Materials Research, Tohoku University, Japan (Project No.16H0023). The synchrotron soft x-ray measurements were performed under User Programs No.2015S2-007 at BL-16A and No.2016PF-BL-19B

at BL-19B, Photon Factory, KEK, Japan. The neutron scattering measurement were performed under User Programs No. 2017A0069 at the Materials and Life Science Experimental Facilities, J-PARC, Japan.

-
- ¹ I. Dzyaloshinsky, J. Phys. Chem. Solids **4**, 241 (1958).
 - ² T. Moriya, Phys. Rev. **120**, 91 (1960).
 - ³ S. Mühlbauer, B. Binz, F. Jonietz, C. Pfleiderer, A. Rosch, A. Neubauer, R. Georgii, and P. Böni, Science **323**, 915 (2009).
 - ⁴ Y. Tokunaga, X. Yu, J. White, H. M. Rønnow, D. Morikawa, Y. Taguchi, and Y. Tokura, Nat. Commun. **6**, 7638 (2015).
 - ⁵ S. Seki, X. Yu, S. Ishiwata, and Y. Tokura, Science **336**, 198 (2012).
 - ⁶ I. Kézsmárki, S. Bordács, P. Milde, E. Neuber, L. Eng, J. White, H. M. Rønnow, C. Dewhurst, M. Mochizuki, K. Yanai, et al., Nat. Mater. **14**, 1116 (2015).
 - ⁷ Y. Fujima, N. Abe, Y. Tokunaga, and T. Arima, Phys. Rev. B **95**, 180410 (2017).
 - ⁸ T. Kurumaji, T. Nakajima, V. Ukleev, A. Feoktystov, T. Arima, K. Kakurai, and Y. Tokura, Phys. Rev. Lett. **119**, 237201 (2017).
 - ⁹ A. K. Nayak, V. Kumar, T. Ma, P. Werner, E. Pippel, R. Sahoo, F. Damay, U. K. Rößler, C. Felser, and S. S. Parkin, Nature (London) **548**, 561 (2017).
 - ¹⁰ S. Seki, S. Ishiwata, and Y. Tokura, Phys. Rev. B **86**, 060403 (2012).
 - ¹¹ E. Ruff, S. Widmann, P. Lunkenheimer, V. Tsurkan, S. Bordács, I. Kézsmárki, and A. Loidl, Sci. Adv. **1**, e1500916 (2015).
 - ¹² G.-H. Cai, M. Greenblatt, and M.-R. Li, Chem. Mater. **29**, 5447 (2017).
 - ¹³ I. Živković, K. Prša, O. Zaharko, and H. Berger, J. Phys.: Condens. Matter **22**, 056002 (2010).
 - ¹⁴ Y. S. Oh, S. Artyukhin, J. J. Yang, V. Zapf, J. W. Kim, D. Vanderbilt, and S.-W. Cheong, Nat. Commun. **5**, 3201 (2014).
 - ¹⁵ J. W. Kim, S. Artyukhin, E. D. Mun, M. Jaime, N. Harrison, A. Hansen, J. Yang, Y. S. Oh, D. Vanderbilt, V. S. Zapf, et al., Phys. Rev. Lett. **115**, 137201 (2015).
 - ¹⁶ M. Yokosuk, A. Al-Wahish, S. Artyukhin, K. O'Neal, D. Mazumdar, P. Chen, J. Yang, Y. S. Oh, S. A. McGill, K. Haule, et al., Phys. Rev. Lett. **117**, 147402 (2016).

- ¹⁷ S. A. Ivanov, R. Mathieu, P. Nordblad, R. Tellgren, C. Ritter, E. Politova, G. Kaleva, A. Mo-sunov, S. Stefanovich, and M. Weil, Chem. Mater. **25**, 935 (2013).
- ¹⁸ K. A. Ross, M. Bordelon, G. Terho, and J. R. Neilson, Phys. Rev. B **92**, 134419 (2015).
- ¹⁹ A. Bogdanov and D. Yablonskii, Zh. Eksp. Teor. Fiz **95**, 182 (1989).
- ²⁰ T. Kimura, T. Goto, H. Shintani, K. Ishizaka, T. Arima, and Y. Tokura, Nature (London) **426**, 55 (2003).
- ²¹ M. Weil, R. Mathieu, P. Nordblad, and S. Ivanov, Cryst. Res. Technol. **49**, 142 (2014).
- ²² M. Prosnikov, A. Smirnov, V. Y. Davydov, Y. Araki, T. Arima, and R. Pisarev, Phys. Rev. B **100**, 144417 (2019).
- ²³ X. Wang, F.-T. Huang, J. Yang, Y. S. Oh, and S.-W. Cheong, APL Mater. **3**, 076105 (2015).
- ²⁴ Y. Yamasaki, T. Sudayama, J. Okamoto, H. Nakao, M. Kubota, and Y. Murakami, J. Phys.: Conf. Ser. **425**, 132012 (2013).
- ²⁵ Y. Yamasaki, D. Morikawa, T. Honda, H. Nakao, Y. Murakami, N. Kanazawa, M. Kawasaki, T. Arima, and Y. Tokura, Phys. Rev. B **92**, 220421 (2015).
- ²⁶ S.-i. Takata, J.-i. Suzuki, T. Shinohara, T. Oku, T. Tominaga, K. Ohishi, H. Iwase, T. Nakatani, Y. Inamura, T. Ito, et al., JPS Conf. Proc. **8**, 036020 (2015).
- ²⁷ Y. Tokura, S. Seki, and N. Nagaosa, Rep. Prog. Phys. **77**, 076501 (2014).
- ²⁸ C. Pappas, Physics **5**, 28 (2012).
- ²⁹ C. Ederer and N. A. Spaldin, Phys. Rev. B **71**, 060401 (2005).
- ³⁰ M. Tokunaga, M. Akaki, T. Ito, S. Miyahara, A. Miyake, H. Kuwahara, and N. Furukawa, Nat. Commun. **6**, 5878 (2015).
- ³¹ The length of DM vector \mathbf{D}_1 is different from that of \mathbf{D}_2 , because of the distinct local atom arrangement.
- ³² K.-L. Ji, E. Solana, A. M. A. Lopez, P. Manuel, C. Ritter, A. Senyshyn, and P. Attfield, Chem. Commun. **54**, 12523 (2018).
- ³³ H. Katsura, N. Nagaosa, and A. V. Balatsky, Phys. Rev. Lett. **95**, 057205 (2005).
- ³⁴ T. Arima, J. Phys. Soc. Jpn. **76**, 073702 (2007).